Phase Diagram of the Topological Superfluid ^{3}He Confined in a Nanoscale Slab Geometry

L. V. Levitin *et al.*

Science **340**, 841 (2013);
DOI: 10.1126/science.1233621

17. S. S. Chng *et al.*, *Science* **337**, 1665 (2012).
18. J. Sohn, R. A. Grant, R. T. Sauer, *Cell* **131**, 572 (2007).
19. Calculations assume 2×10^6 LPS molecules per *E. coli* cell, a doubling time of 30 min, and a periplasmic volume of 3×10^{-16} liters.
20. J. E. Mogensen, D. E. Otzen, *Mol. Microbiol.* **57**, 326 (2005).
21. C. L. Hagan, T. J. Silhavy, D. Kahne, *Annu. Rev. Biochem.* **80**, 189 (2011).
22. G. F. Ames, E. N. Spudich, H. Nikaido, *J. Bacteriol.* **117**, 406 (1974).
23. E. A. Austin, J. F. Graves, L. A. Hite, C. T. Parker, C. A. Schnaitman, *J. Bacteriol.* **172**, 5312 (1990).
24. H. Nikaido, *Microbiol. Mol. Biol. Rev.* **67**, 593 (2003).
25. D. Vertommen, N. Ruiz, P. Leverrier, T. J. Silhavy, J. F. Collet, *Proteomics* **9**, 2432 (2009).
26. B. M. Alba, H. J. Zhong, J. C. Pelayo, C. A. Gross, *Mol. Microbiol.* **40**, 1323 (2001).

Acknowledgments: We thank B. Cezairliyan, S. Chng, D. Kahne, C. Raetz, and D. Six for discussions and strains. Supported by NIH grants AI-16892 and GM-36278. S.L. was supported by an NIH postdoctoral fellowship (AI-084442). The data reported in this paper are presented in the main text and supplementary materials.

Supplementary Materials
www.sciencemag.org/cgi/content/full/340/6134/837/DC1
Materials and Methods
Figs. S1 to S12
Table S1
References (*27*–*32*)

18 January 2013; accepted 25 March 2013
10.1126/science.1235358

Phase Diagram of the Topological Superfluid ^{3}He Confined in a Nanoscale Slab Geometry

L. V. Levitin,[1] R. G. Bennett,[1]* A. Casey,[1] B. Cowan,[1] J. Saunders,[1]† D. Drung,[2] Th. Schurig,[2] J. M. Parpia[3]

The superfluid phases of helium-3 (^{3}He) are predicted to be strongly influenced by mesoscopic confinement. However, mapping out the phase diagram in a confined geometry has been experimentally challenging. We confined a sample of ^{3}He within a nanofluidic cavity of precisely defined geometry, cooled it, and fingerprinted the order parameter using a sensitive nuclear magnetic resonance spectrometer. The measured suppression of the p-wave order parameter arising from surface scattering was consistent with the predictions of quasi-classical theory. Controlled confinement of nanofluidic samples provides a new laboratory for the study of topological superfluids and their surface- and edge-bound excitations.

At temperatures close to absolute zero, helium-3 (^{3}He) becomes a superfluid, a state of matter exhibiting macroscopic quantum coherence and characterized by dissipationless flow. A number of superfluid phases emerge that have a rich variety of broken symmetries and nontrivial momentum-space topologies (*1*–*4*). They provide model systems for unconventional superconductivity (*5*) and embody key paradigms of topological quantum matter (*6*, *7*). The quantum liquid ^{3}He played the central role in the establishment of Landau Fermi liquid theory, which describes a degenerate system of mobile strongly interacting fermions as weakly correlated quasi-particles. Superfluidity in liquid ^{3}He arises from the formation of Cooper pairs, with relative orbital angular momentum $L = 1$ (p-wave) and total spin $S = 1$ (^{3}He has nuclear spin 1/2). The Balian-Werthamer (B) phase is a time-reversal-invariant p-wave superfluid (*8*), analogous to topological insulators and quantum spin Hall systems (*9*, *10*). The Anderson-Brinkman-Morel (A) phase is a chiral p-wave superfluid, breaking time-reversal symmetry, and in the two-dimensional limit is analogous to integer quantum Hall systems (*3*) and related to the candidate topological superconductor Sr_2RuO_4 (*6*, *11*).

Dimensional confinement into a film geometry of this model system for superconducting/superfluid p-wave order is predicted to give rise to considerable surface-induced distortions of the order parameter (*12*). The relevant confinement length scale is set by the diameter of the Cooper pair, $\xi_0 = \hbar v_F/2\pi k_B T_c$, where v_F is the Fermi velocity, T_c is the superfluid transition temperature, $\hbar$ is Planck's constant h divided by 2π, and k_B is the Boltzmann constant; $\xi_0 = 75$ nm at zero pressure, where $T_c = 0.9$ mK. The topological nature of the superfluids leads to Majorana (*13*) or Majorana-Weyl fermionic excitations at surfaces (*14*) or edges (*3*, *15*) of the B and A phases respectively. The order parameter distortions and spectral weight of surface excitations are directly related and may be predicted by quasi-classical theory (*16*). Nevertheless, our understanding of the superfluid order of a ^{3}He film has remained limited, constrained by the difficulty in experimentally fingerprinting the order parameter of a film of precisely defined thickness; addressing this challenge is the central thrust of this Report.

In previous work, the superfluid flow of a thin liquid film over highly polished metal surfaces has been observed (*17*). The excitation of surface waves (third sound) (*18*) and torsional oscillator methods (*19*) have been used to determine the superfluid density as a function of film thickness. However, these methods crucially were unable to identify the pairing state. Moreover, achieving uniformity of the film and measuring the film thickness precisely are experimentally challenging.

These issues are addressed in our experiment by confining superfluid ^{3}He within a single nanofabricated cavity. The key control parameter, cavity height (which determines the film thickness), is fully characterized. We were able to cool such samples to well below 1 mK and interrogated them by means of nuclear magnetic resonance (NMR) in order to fingerprint the superfluid ^{3}He order parameter. We have developed an ultrasensitive NMR spectrometer (*20*) to detect signals from this tiny sample. These technical steps represent a critical advance on previous NMR studies of confined ^{3}He, in which an ensemble of typically 1000 films within a stack of plastic sheets separated by spacer particles has been investigated (*21*), leading to an undesirably broad distribution of film thickness.

The sample geometry is shown in Fig. 1. We have investigated the pressure range from 0 to 5.5 bar, over which the Cooper pair diameter ξ_0 decreased by approximately a factor of two, providing pressure tuning of the effective confinement for a fixed cavity height D. The temperature dependence of the effective confinement is determined by the ratio of D to the temperature-dependent superfluid coherence length $\xi(T)$. The coherence length determines the scale of the recovery of the order parameter away from the surface and arises from the competition between condensation and order parameter gradient energies (*12*). In this work, we define $\xi_\Delta(T) = \hbar v_F/\Delta_B(T)\sqrt{10}$, where $\Delta_B(T)$ is the bulk B-phase gap, $\xi_\Delta(0) = 1.13\xi_0$, and $\xi_\Delta(T)$ diverges approaching T_c (*22*).

The p-wave superfluid order is represented as the amplitudes of pairs with projections of orbital and spin angular momentum L_z, $S_z = 1, 0, -1$; corresponding terms in the momentum-space pair-wavefunction $\mathbf{\Delta(p)}$ have orbital part $(\hat{p}_x + i\hat{p}_y)$,

[1]Department of Physics, Royal Holloway University of London, Egham, Surrey, TW20 0EX, UK. [2]Physikalisch-Technische Bundesanstalt, Abbestrasse 2-12, D-10587 Berlin, Germany. [3]Department of Physics, Cornell University, Ithaca, NY 14853, USA.

*Present address: Isentropic Ltd, 7, Brunel Way, Segensworth East, Hampshire PO15 5TX, UK.
†Corresponding author. E-mail: j.saunders@rhul.ac.uk

$\sqrt{2}\hat{p}_z$, and $(-\hat{p}_x + i\hat{p}_y)$ and spin part $|\uparrow\uparrow\rangle$, $[|\uparrow\downarrow\rangle + |\downarrow\uparrow\rangle]/\sqrt{2}$, and $|\downarrow\downarrow\rangle$, respectively (*3*). Those pairs with orbital angular momentum in the plane of the cavity surface ($L_z = 0$) are completely suppressed at the surface (*12*). There is weaker or no suppression of pairs with orbital angular momentum parallel to the cavity surface normal $L_z = \pm 1$, depending on the nature of surface scattering. The spatial dependence of the components of the order parameter across the cavity is predicted within the framework of quasi-classical theory (*23*, *24*).

The identification of the phases of superfluid ^{3}He is possible through NMR spectroscopy, which directly probes the spin degrees of freedom of the Cooper pairs (*22*). Although the condensation energy of Cooper pairing is invariant under relative rotation of the spin and orbital axes of the pairs, spin-orbit symmetry is broken by the nuclear dipole-dipole interaction of the paired fermions. This weak spin-orbit coupling energy leads to a frequency shift of the NMR spectrum with respect to the normal state and provides a signature of the superfluid order. This effect played the central role in the identification of the phases of bulk superfluid ^{3}He shortly after their discovery (*1*).

At the pressure of 2.2 bar (Fig. 2), only the A phase is observed, with the order parameter $\Delta(\mathbf{p}) = \Delta(z)(\hat{p}_x + i\hat{p}_y)[|\uparrow\uparrow\rangle + |\downarrow\downarrow\rangle]$, where $\Delta(z)$ denotes that the gap has a spatial dependence across the cavity. This is a state with just the $S_z = \pm 1$ components of the spin triplet. The orbital angular momentum of all pairs is aligned and oriented normal to the cavity surface $\mathbf{l} = \pm\,\hat{\mathbf{z}}$. The gap is suppressed with respect to the bulk A-phase gap for surfaces that scatter quasi-particles diffusively (randomly); specular scattering is predicted to eliminate this suppression (*24*). The static magnetic field $\mathbf{B}_0 = B_0\hat{\mathbf{z}}$ orients the spins along $\hat{\mathbf{z}}$, via the nuclear Zeeman energy, which for $B_0 = 32$ mT used in our experiment is larger than the spin-orbit coupling. This configuration maximizes the dipolar energy and gives rise to the observed negative frequency shift (*25*).

At 5.5 bar, on cooling through the superfluid transition, we first observed a similar A-phase signature, followed by a transition into a low-temperature phase. This phase is predicted to be the planar-distorted B phase (*23*, *24*), with order parameter $\Delta(\mathbf{p}) = \Delta_{||}(z)(-\hat{p}_x + i\hat{p}_y)|\uparrow\uparrow\rangle + \Delta_{||}(z)(\hat{p}_x + i\hat{p}_y)|\downarrow\downarrow\rangle + \Delta_{\perp}(z)\hat{p}_z[|\uparrow\downarrow\rangle + |\downarrow\uparrow\rangle]$, with all three components of the spin and orbital triplets; in the expression above, $L_z = -S_z$. The bulk B phase is described by the above expression with isotropic gap: $\Delta_{\perp} = \Delta_{||}$. However, the cavity is predicted to induce a spatially dependent gap distortion: $\Delta_{\perp}(z) < \Delta_{||}(z)$. The order parameter component describing the $L_z = 0$ pairs changes sign upon quasi-particle reflection at the boundary, leading to the complete suppression of $\Delta_{\perp}$ approaching the walls and the formation of surface-bound states (*26*). Similar pair-breaking occurs in unconventional superconductors—for example, at the [110] surface of a cuprate superconductor with $d_{x^2-y^2}$ symmetry—for this reason (*27*).

Entering this phase, we found the sample in a state with either a positive (B_+) or negative (B_-) frequency shift; sometimes both signatures were observed at once, in which case, the sample is understood to comprise B_+ and B_- domains. The two NMR signatures are attributed to different

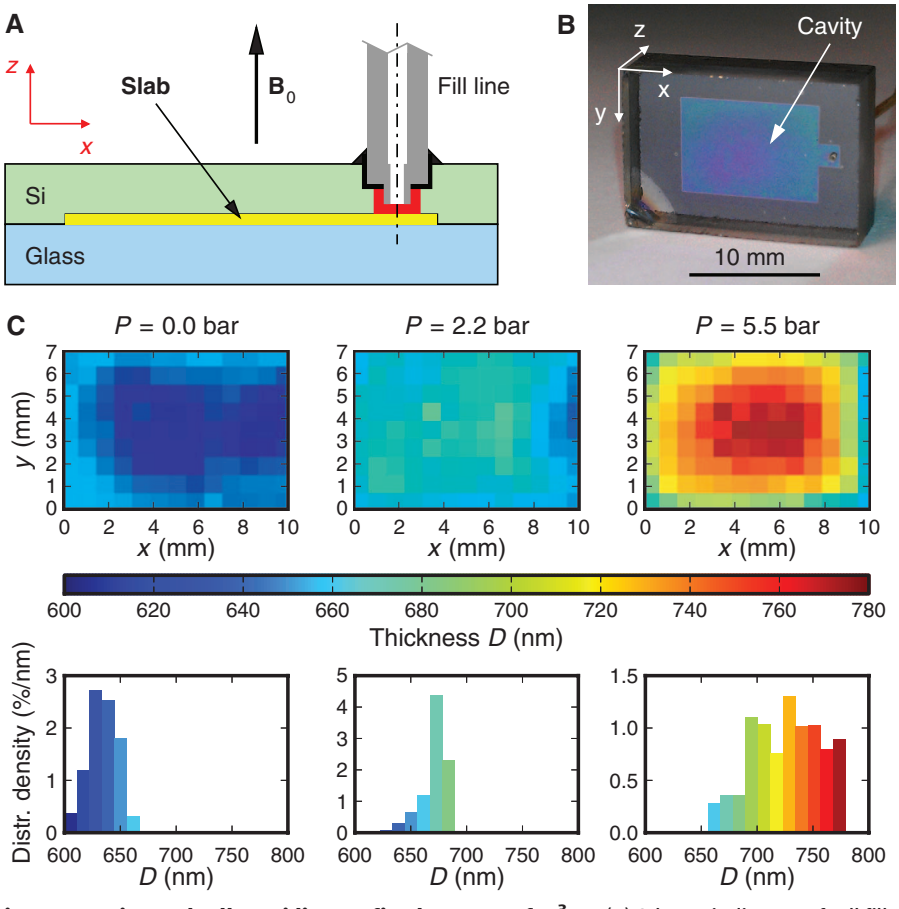

Fig. 1. Experimental cell providing confined geometry for ^{3}He. (**A**) Schematic diagram of cell filled with helium. The cell is fabricated from glass (blue) and silicon (green) wafers anodically bonded together. The unsupported cavity, of designed thickness 650 nm, is defined lithographically in the silicon wafer. A silver fill line (gray) is fitted with epoxy (black) through a hole drilled in the silicon. Yellow represents the slab of confined helium being investigated with NMR in a static field $B_0 = 32$ mT normal to the slab, and red is the small amount of bulk liquid around the mouth of the fill line also observed with the NMR spectrometer (*22*). (**B**) A photograph of the cell. (**C**) Slab thickness profiles and distributions determined at low temperatures and three sample pressures by means of optical interferometry.

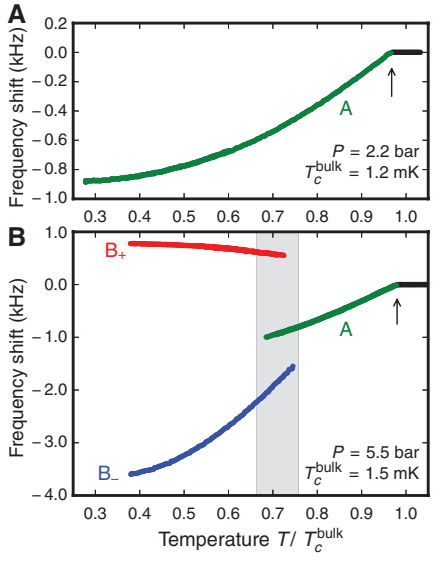

Fig. 2. NMR frequency shift signatures of superfluidity in the slab. (**A**) At 2.2 bar, a second-order phase transition (vertical arrow) is observed in the cavity between the normal state, in which the NMR precession occurs at the Larmor frequency, and the superfluid A phase, with a negative frequency shift. The superfluid transition temperature in the cavity is suppressed relative to that in bulk liquid T_c^{bulk}. (**B**) At 5.5 bar, there is also a first-order phase transition on cooling from the A phase to the planar-distorted B phase. The B phase has two possible configurations, B_+ and B_-, with positive and negative frequency shift, respectively. On cooling from the A phase, we observed either configuration or both, stochastically. The data are a compilation of several temperature sweeps. There is a region of coexistence of A and B phases around the A-B transition (gray). Data were obtained with diffuse walls.

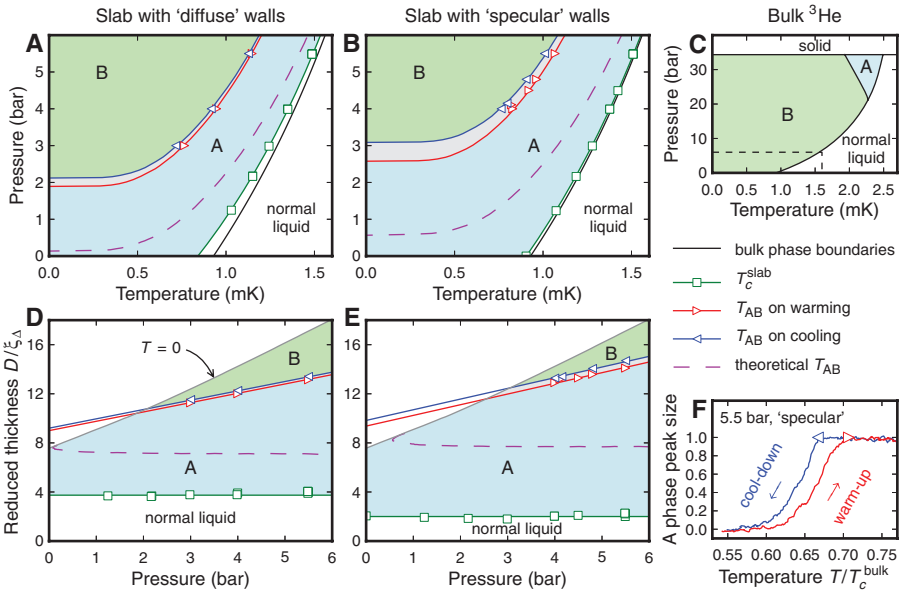

Fig. 3. Phase diagram of superfluid ^{3}He in the slab. (**A** and **B**) Phase diagram in the cavity with (A) diffuse and (B) specular walls. A-B phase boundary corresponds to the maximum cavity height at each pressure. (**C**) Bulk superfluid ^{3}He phase diagram (*2*) shown for comparison, in which the dashed region indicates the pressure range covered in plots (A) and (B). (**D** and **E**) Phase diagrams (A) and (B) respectively mapped into the reduced thickness $D/\xi_\Delta(T, P)$ versus pressure P plane (*22*) showing the boundary condition dependence of the superfluid transition temperature in the cavity T_c^{slab} and the A to planar-distorted-B transition temperature T_{AB}. The lines through the data are linear fits and are used to extrapolate the A-B phase boundary in the P-T plane in (A) and (B). The $T = 0$ value of $D/\xi_\Delta(T, P)$ is also shown (gray). The purple dashed line in (A) to (E) is the A-B phase boundary predicted by weak-coupling quasi-classical theory (*30*). (**F**) Signature of the A-B transition, from peak size of A-phase NMR line, on warming and cooling. The observed width of the transition is attributed to the slab thickness distribution. The features marked by triangles, observed on cooling and warming, are assigned to the maximum cavity thickness (*22*). Both cooling and warming data for the A-B transition are plotted in (A) to (E), placing bounds on the equilibrium transition temperature.

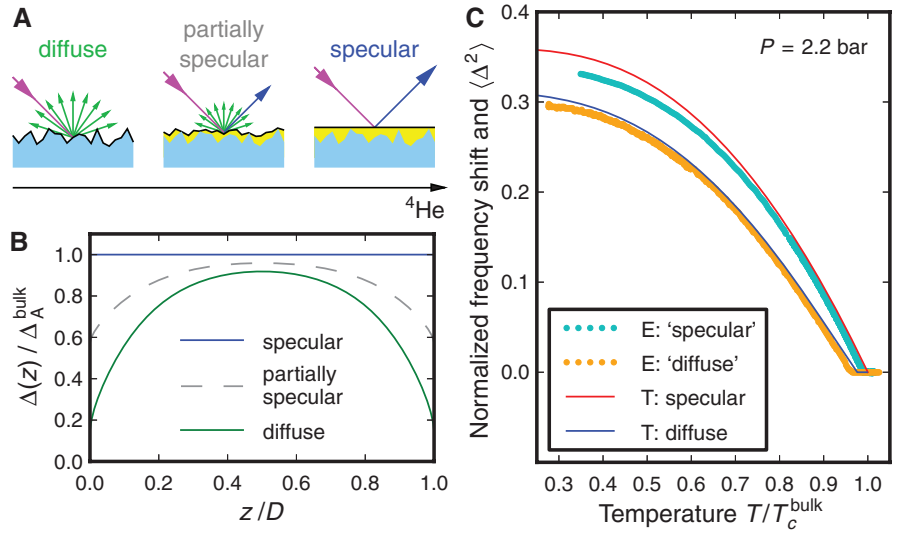

Fig. 4. Measured gap suppression in A phase and its dependence on boundary condition. (**A**) Quasi-particle scattering at boundary can be tuned from diffuse to specular by varying the thickness of a surface ^{4}He film (yellow). (**B**) Typical calculated A-phase gap profile for different boundaries (*22*–*24*). (**C**) Spatially averaged gap inferred from experimentally measured frequency shift (E) in comparison with results from quasi-classical theory (T) (*24*). The data are scaled so that the slope at T_c for specular scattering is unity (*22*).

relative spin-orbit orientations of the planar-distorted B phase (*28*). The positive shift corresponds to the orientation $L_z = -S_z$ presented above, for which both the nuclear Zeeman and spin-orbit energies are minimized. In the presence of confinement, the gap distortion induces an anisotropic magnetic susceptibility. As a result, a configuration of the B phase with $L_z = S_z$ may also be stabilized by the Zeeman energy, with order parameter $\Delta(\mathbf{p}) = \Delta_{||}(z)(-\hat{p}_x + i\hat{p}_y)|\downarrow\downarrow\rangle + \Delta_{||}(z)(\hat{p}_x + i\hat{p}_y)|\uparrow\uparrow\rangle + \Delta_\perp(z)\hat{p}_z[|\uparrow\downarrow\rangle + |\downarrow\uparrow\rangle]$. This state has a higher spin-orbit energy and a negative frequency shift. Because the planar-distorted B phase is nucleated at the first-order transition from the A phase, and the B_+ and B_- configurations only differ energetically via the weak spin-orbit coupling energy, we observed an arbitrary distribution of B_+ and B_- domains.

Confinement in the slab has a profound effect on the superfluid phase diagram (Fig. 3, A and B), as predicted theoretically (*24*, *29*, *30*). In bulk liquid ^{3}He in zero magnetic field, the equilibrium A phase exists only at high pressure, as a result of strong-coupling effects (Fig. 3C) (*1*, *2*). Under confinement, a large area of the P-T plane at low pressures is opened up in which the A phase is stable. This arises from the weaker order parameter suppression of the A phase relative to the B phase owing to the absence of pairs with $L_z = 0$. The observed A-B transition occurs over a range of temperatures on both cooling and warming, arising from the distribution of cavity thickness. In addition, there is hysteresis between data taken on warming and cooling (Fig. 3F) that we tentatively attribute to pinning of the A-B boundary at scratches on the cell walls. The boundary conditions may be tuned in situ by plating the surface with ^{4}He because a thin superfluid ^{4}He layer is found to produce close to specular scattering (*21*). We have performed studies for two boundary conditions, denoted "diffuse" and "specular," close to the diffuse and specular limits (*22*). We found that specular boundaries extend somewhat the region of stability of the A phase, as expected theoretically. They substantially reduce the suppression of the film superfluid transition temperature. The A-B phase boundary, mapped into the $D/\xi_\Delta(T, P)$ versus pressure plane (Fig. 3, D and E), reveals both a pressure-dependence and a shift relative to the predicted weak-coupling phase boundary (*30*). These observations are evidence for strong-coupling effects that persist to zero pressure.

We can measure the suppression of the A-phase gap, and its dependence on quasi-particle scattering boundary conditions, because the NMR frequency shift $|\Delta f| \propto \langle\Delta^2(z)\rangle$. Analysis of the frequency shift (Fig. 4) indicates good agreement with quasiclassical theory for the gap suppression by diffusely scattering walls (*24*) and demonstrates its predictive power.

Our results open the prospects for tailoring mesoscopic confinement and surface scattering both for the investigation of excitations in known topological superfluids and for the discovery of

new superfluid states. In particular, the environment may be optimized for the detection of Majorana fermions at the surface of ^{3}He-B and the Majorana-Weyl edge modes in chiral ^{3}He-A (*31*). Predicted new p-wave superfluids include a quasi–two-dimensional version of ^{3}He-A (a gapped $p_x + ip_y$ superfluid) (*3*) and a spatially modulated phase (*32*). Such experiments on dimensionally confined superfluid ^{3}He provide flexible model systems, when coupled with quasi-classical theory, for understanding topological superfluidity. This is likely to have considerable impact on the emerging field of topological quantum matter.

References and Notes

1. A. J. Leggett, *Rev. Mod. Phys.* **47**, 331 (1975).
2. D. Vollhardt, P. Wölfle, *The Superfluid Phases of ^{3}He* (Taylor & Francis, London, UK, 1990).
3. G. Volovik, *Exotic Properties of Superfluid ^{3}He* (World Scientific, Singapore, 1992).
4. G. Volovik, *The Universe in a Helium Droplet* (Oxford Univ. Press, London, 2002).
5. M. R. Norman, *Science* **332**, 196 (2011).
6. X.-L. Qi, S.-C. Zhang, *Rev. Mod. Phys.* **83**, 1057 (2011).
7. J. E. Moore, *Nature* **464**, 194 (2010).
8. R. Roy, http://arxiv.org/abs/0803.2868.
9. X.-L. Qi, T. L. Hughes, S. Raghu, S.-C. Zhang, *Phys. Rev. Lett.* **102**, 187001 (2009).
10. A. P. Schnyder, S. Ryu, A. Furusaki, A. W. W. Ludwig, *Phys. Rev. B* **78**, 195125 (2008).
11. A. P. Mackenzie, Y. Maeno, *Rev. Mod. Phys.* **75**, 657 (2003).
12. V. Ambegaokar, P. G. de Gennes, D. Rainer, *Phys. Rev. A* **9**, 2676 (1974).
13. F. Wilczek, *Nat. Phys.* **5**, 614 (2009).
14. S. B. Chung, S.-C. Zhang, *Phys. Rev. Lett.* **103**, 235301 (2009).
15. M. Stone, R. Roy, *Phys. Rev. B* **69**, 184511 (2004).
16. J. W. Serene, D. Rainer, *Phys. Rep.* **101**, 221 (1983).
17. S. Steel, J. P. Harrison, P. Zawadski, A. Sachrajda, *J. Low Temp. Phys.* **95**, 759 (1994).
18. A. M. R. Schechter, R. W. Simmonds, R. E. Packard, J. C. Davis, *Nature* **396**, 554 (1998).
19. J. Xu, B. C. Crooker, *Phys. Rev. Lett.* **65**, 3005 (1990).
20. L. V. Levitin *et al.*, *Appl. Phys. Lett.* **91**, 262507 (2007).
21. M. R. Freeman, R. S. Germain, E. V. Thuneberg, R. C. Richardson, *Phys. Rev. Lett.* **60**, 596 (1988).
22. Materials and methods are available as supplementary materials on *Science* Online.
23. Y. Nagato, M. Yamamoto, K. Nagai, *J. Low Temp. Phys.* **110**, 1135 (1998).
24. A. B. Vorontsov, J. A. Sauls, *Phys. Rev. B* **68**, 064508 (2003).
25. A. I. Ahonen, M. Krusius, M. A. Paalanen, *J. Low Temp. Phys.* **25**, 421 (1976).
26. L. J. Buchholtz, G. Zwicknagl, *Phys. Rev. B* **23**, 5788 (1981).
27. C.-R. Hu, *Phys. Rev. Lett.* **72**, 1526 (1994).
28. Yu. M. Bunkov, G. E. Volovik, *Sov. Phys. JETP* **76**, 794 (1993).
29. L. H. Kjäldman, J. Kurkijärvi, D. Rainer, *J. Low Temp. Phys.* **33**, 577 (1978).
30. Y. Nagato, K. Nagai, *Physica B* **284-288**, 269 (2000).
31. J. A. Sauls, *Phys. Rev. B* **84**, 214509 (2011).
32. A. B. Vorontsov, J. A. Sauls, *Phys. Rev. Lett.* **98**, 045301 (2007).

Acknowledgments: We thank S. Dimov, B. Ilic, and S. S. Verbridge for assistance with cell construction at Cornell Nano Fabrication Facility; S. T. Boogert and A. Bosco for advice and loan of equipment for optical thickness measurement; and M. Eschrig for critically reading the manuscript. This work was supported by Engineering and Physical Sciences Research Council grants EP/C522877/1, EP/E0541129/1, and EP/J022004/1; NSF grants DMR-0806629 and DMR-120991; and European Microkelvin Consortium (FP7 grant agreement 228464). We dedicate this paper to the memory of Professor Robert C. Richardson (1937–2013), who inspired this research.

Supplementary Materials

www.sciencemag.org/cgi/content/full/340/6134/841/DC1
Materials and Methods
Figs. S1 to S14
Table S1
References (*33*–*49*)

4 December 2012; accepted 11 March 2013
10.1126/science.1233621

3D Computational Imaging with Single-Pixel Detectors

B. Sun,[1]* M. P. Edgar,[1] R. Bowman,[1,2] L. E. Vittert,[3] S. Welsh,[1] A. Bowman,[3] M. J. Padgett[1]

Computational imaging enables retrieval of the spatial information of an object with the use of single-pixel detectors. By projecting a series of known random patterns and measuring the backscattered intensity, it is possible to reconstruct a two-dimensional (2D) image. We used several single-pixel detectors in different locations to capture the 3D form of an object. From each detector we derived a 2D image that appeared to be illuminated from a different direction, even though only a single digital projector was used for illumination. From the shading of the images, the surface gradients could be derived and the 3D object reconstructed. We compare our result to that obtained from a stereophotogrammetric system using multiple cameras. Our simplified approach to 3D imaging can readily be extended to nonvisible wavebands.

Computational imaging based on projected patterns is an alternative technique to conventional imaging and removes the need for a spatially resolving detector. Instead, this form of computational imaging infers the scene by correlating the known spatial information of a changing incident light field with the total reflected (or transmitted) intensity. For example, two copies of a randomly generated light field can be made with a beam splitter; one copy of the light field interacts with the object and a non–spatially resolving detector, and the other copy is recorded with a camera. Aggregating the correlations between the two detectors yields an image even though the light striking the camera has never interacted with the object. This phenomenon, called ghost imaging, has been demonstrated in both the quantum and classical regimes (*1*–*9*).

Such imaging systems can be simplified by using a device capable of generating computer-programmable random light fields, which obviates the requirement for the beam splitter and the camera because knowledge of the light field is held in the computer memory. This type of system was initially called computational ghost imaging (*10*) but is similar in approach to more standard computational imaging systems, which use projected light patterns [albeit usually highly structured (*11*, *12*)]. We also note that the use of projected patterns is related to the field of single-pixel cameras (*13*), where the programmable component is used to filter the detected, rather than illuminating, light.

In both single-pixel cameras and computational imaging systems, inverting the known random patterns and the measured intensities is a computational problem. A number of sophisticated algorithms have been developed over the years to improve the signal-to-noise ratio (SNR) for different systems (*14*, *15*), but with appropriate normalization (*16*) a simple iterative algorithm was adopted for this experiment.

Previous experiments in single-pixel computational imaging (*9*, *14*, *16*) were restricted to relatively small (less than 10 cm) two-dimensional (2D) images, mainly of 2D template objects or 2D outlines of 3D objects. In the present work, we capture the 3D spatial form of an object by using several single-pixel detectors in different locations. A 2D image is derived from each detector but appears as if it is illuminated differently from the others. Comparing the shading information in the images allows the surface gradient and hence the 3D form of the surface to be reconstructed.

The experimental setup (Fig. 1) consists of a digital light projector to illuminate objects with random binary light patterns, four spatially separated single-pixel photodetectors to measure the intensity of the reflected light, an analog-to-digital converter to digitize the photodetector signals, and a computer to generate the random speckle pattern as well as perform 3D reconstructions of the test object.

The digital light projector comprises a red, green, and blue light-emitting diode illumination source and a digital micromirror device (DMD) to generate the structured illumination

[1]Scottish Universities Physics Alliance, School of Physics and Astronomy, University of Glasgow, Glasgow G12 8QQ, UK. [2]Department of Physics, Cavendish Laboratory, University of Cambridge, Cambridge CB3 0HE, UK. [3]School of Mathematics and Statistics, University of Glasgow, Glasgow G12 8QQ, UK.

*Corresponding author. E-mail: b.sun.1@research.gla.ac.uk